Orientational order parameters of a de Vries–type ferroelectric liquid crystal obtained by polarized Raman spectroscopy and x-ray diffraction

A. Sanchez-Castillo, M. A. Osipov, S. Jagiella, Z. H. Nguyen, M. Kašpar, V. Hamplovă, J. Maclennan, and F. Giesselmann

Orientational order parameters of a de Vries-type ferroelectric liquid crystal obtained by polarized Raman spectroscopy and x-ray diffraction.

A. Sanchez-Castillo[1], M. A. Osipov[2], S. Jagiella[1], Z. H. Nguyen[3], M. Kašpar[4], V. Hamplová[4], J. Maclennan[3]and F. Giesselmann [1]

[1] *Institut für Physikalische Chemie, Universität Stuttgart, Stuttgart, Germany*
[2] *Department of Mathematics, University of Strathclyde, Glasgow, UK*
[3] *Deparment of Physics and Liquid Crystals Materials Research Center, University of Colorado, Boulder, Colorado, USA*
[4] *Institute of Physics, Academy of Sciences of the Czech Republic, Prague, Czech Republic*

ABSTRACT

The orientational order parameters $<P_2>$ and $<P_4>$ of the ferroelectric, de Vries-type liquid crystal 9HL have been determined in the SmA* and SmC* phases by means of polarized Raman spectroscopy, and in the SmA* phase using x-ray diffraction. Quantum density functional theory predicts Raman spectra for 9HL that are in good agreement with the observations and indicates that the strong Raman band probed in the experiment corresponds to the uniaxial, coupled vibration of the three phenyl rings along the molecular long axis. The magnitudes of the orientational order parameters obtained in the Raman and x-ray experiments differ dramatically from each other, a discrepancy that is resolved by considering that the two techniques probe the orientational distributions of different molecular axes. We have developed a systematic procedure in which we calculate the angle between these axes and rescale the orientational order parameters obtained from x-ray scattering with results that are then in good agreement with the Raman data.

At least in the case of 9HL, the results obtained by both techniques support a sugar loaf orientational distribution in the SmA* phase with no qualitative difference to conventional smectics A. The role of individual molecular fragments in promoting de Vries-type behaviour is considered.

I. INTRODUCTION

The smectic A (SmA and for a chiral phase SmA*) phase, which is the simplest smectic phase, is composed of molecules with a rod-like shape stacked in two-dimensional layers. The molecules within each layer create a two-dimensional, liquid-like structure and the quasi-long-range one-dimensional positional order of the molecules associated with the layering can be specified by a density wave with the vector $\mathbf{q}$ parallel to the layer normal $\mathbf{k}$ [1]. Similarly, the director $\mathbf{n}$ is defined as the macroscopic symmetry axis which specifies the orientational order of the molecular long axes (see Fig. 1). The long-range orientational order is described by means of the orientational order parameters (OOP) which specifies the orientational distribution of the long molecular axis around the director $\mathbf{n}$. In the simplest case, the

1

molecules are assumed to possess an effective cylindrical symmetry, and the orientational distribution function $f(\beta)$ of the SmA phase depends only on the Euler angle β between the molecular long axis and the director $\mathbf{n}$. In this case, $f(\beta)$ can be expanded in terms of Legendre polynomials $P_L(\cos\beta)$ with coefficients proportional to the corresponding OOP $<P_L(\cos\beta)>$, the statistical averages of the corresponding Legendre polynomials [2]. The first two statistical averages $<P_2>$ and $<P_4>$ can be measured using various different experimental methods, including polarized Raman spectroscopy (PRS) and x-ray diffraction (XRD) [3-8]. In biaxial phases, the distribution function takes a more general form $f(\beta,\alpha)$, which includes a dependence on the azimuthal Euler angle α and on the biaxial order parameters [2, 9].

The smectic layering in the SmA and SmC phases is characterized by the translational order parameter Σ, the amplitude of the periodic density wave describing the one-dimensional positional order. This set of order parameters, as well as the tilt angle θ in the SmC phase, is sufficient to describe the molecular ordering in smectic phases.
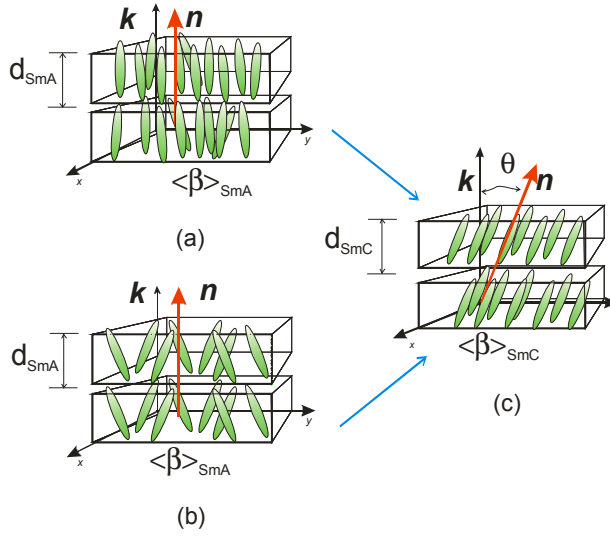

FIG. 1 (Color online) The layer normal $\mathbf{k}$, the director $\mathbf{n}$, the tilt angle and the layer spacing d as well as the molecular average orientation $<\beta>$ are illustrated. a) Shows the conventional picture of the SmA phase. In contrast in b), in the de Vries scenario the molecules are already tilted in the SmA phase and the SmA-SmC occurs as an order-disorder phase transition b) →c). The classical SmA–SmC phase transition is illustrated as a) →c).

In the orthogonal SmA phase, the director $\mathbf{n}$ is parallel to the layer normal $\mathbf{k}$ whereas in the SmC phase, $\mathbf{n}$ is tilted by an angle θ with respect to $\mathbf{k}$ (see Fig. 1). With decreasing temperature below the SmA–SmC transition, the director $\mathbf{n}$ gradually tilts with respect to $\mathbf{k}$, and a noticeable layer contraction of the smectic layers is usually observed, *i.e.* the layer spacing in the SmC phase is smaller than that in the SmA phase, $d_{SmC} < d_{SmA}$ [10-12]. In this case the layer contraction is determined by the average tilt of molecular long axes. It is worth noting, however, that even in the conventional smectic A phase a given molecule is most probably tilted at any moment of time since typical values of $<P_2>$ for the SmA phase are in range 0.7 - 0.9, *i.e.* the value of $<P_2>$ is always less than one [13, 14]. This effect can be explained in terms of the thermal orientatonal fluctuations present in any molecular system. Therefore, in most cases the layer spacing d is somewhat smaller than the molecular length L even in the SmA phase of a conventional smectic material.

In the de Vries scenario, the molecules are already tilted in the SmA phase but the particular direction of the tilt is not specified and the phase is characterised by short range azimuthal correlations of the molecular axes. In the vicinity of the SmA–SmC transition these azimuthal correlations become long-ranged, and an order-disorder transition is observed [15-18]. The transition is accompanied by a small or almost nonexistent smectic layer contraction, $d_{SmA} \approx d_{SmC}$. Additional features are observed in chiral smectic liquid crystals of de Vries-type. First, a very strong electroclinic effect is usually observed in the SmA* phase close to the transition into the SmC* phase [19-20]. Secondly, strong soft mode fluctuations in the vicinity of the SmA*–SmC* transition distinguish such materials from conventional smectics [11, 12, 14, 18, 21]. These characteristics are typical for chiral de Vries materials studied so far but, at the same time, the particular microscopic mechanism driving the de Vries-type SmA–SmC (SmA*–SmC*) transition is not fully understood.

Orientational order parameters of different de Vries-type smectic materials have been determined experimentally using birefringence technique as well as Raman and Infrared spectroscopy (IR). Hayashi *et al.* used polarized Raman spectroscopy (PRS) and IR to study the well known de Vries-type siloxane terminated liquid crystal TSiKN65 [22, 23]. Their experiments yielded extremely low values of the OOP, a result they argued could be explained by taking into account the particular molecular structure. They concluded that the apparently low values of the order parameters are mainly determined by the large angle $\beta_c \approx 26°$ between the molecular core and the long molecular axis which is the primary axis of the molecular inertia tensor. After making the corresponding correction to the model, the real values of the OOP for TSiKN65 appeared to be significantly higher than those measured [23]. Nevertheless, the OOP were still relatively low compared to the typical values obtained in conventional smectics. This indicates that a more consistent study of the OOP must include an analysis of the particular molecular structure.

Another useful method which has been used to determine the values $<P_2>$ and $<P_4>$ in de Vries-type materials is x-ray scattering diffraction [3, 4, 7, 24]. X-ray diffraction originates from the interaction between the electron density distribution of molecules and the x-ray beam [25], while the scattered Raman signal is the response of the inelastic interaction between the molecular polarizability tensor and the beam of light [26]. Consequently, x-ray and Raman experiments probe the molecular ordering in completely different ways. The two methods are expected to yield similar results for the OOP only if the particular Raman vibration axis of the molecule coincides with the axis of the effective uniaxial structure, which is obtained by a rotation of the whole molecule about the primary axis of the molecular inertial tensor.

The ferroelectric liquid crystal (FLC) (*S*)-hexyl-lactate compound denoted as 9HL [27], which exhibits a SmA*–SmC* transition of the second order, is the subject of the present study. Previous studies have shown that 9HL exhibits a small layer contraction at the SmA*–SmC* phase transition as well as a big electroclinic response [18]. Dielectric studies showed that 9HL possesses strong soft mode fluctuations in the vicinity of this transition [11]. In addition, a small α value in the coefficients of the Landau expansion, typically observed in de Vries-type materials, was obtained [18]. These results enable one to consider 9HL as a material with de Vries-type properties.

Recent NMR experiments carried out on deuterated 9HL molecules yielded values of $<P_2> \approx 0.8$ which are similar to those found in conventional smectics [28], an unexpected result for a de Vries-type material. A similar tendency has recently been observed in another de Vries-type system by H. Yoon *et al.* using x-ray scattering [29]. In contrast, Chang *et al.* studied FLCs showing a small layer contraction at the SmA*–SmC* transition using PRS and found

3

relative high values of the OOP. Nevertheless, their results showed that the SmA*-SmC* transition is not de Vries-type but rather a SmA*-SmC$_\alpha$* transition [30]. In 9HL, no experimental evidence (optic, electro-optic, x-ray, dielectric) of an intermediate ferroelectric SmC$_\alpha$* phase has been reported [18, 11, 24].

On the other hand, relatively low OOP have been obtained in most of the studies done so far in de Vries-type FLCs. These materials generally possess siloxane- or fluorinate-terminated groups and high smectic order parameters [24, 29, 31]. The nanoscale segregation of such groups is believed to be responsible for the enhancement of the smectic order in these materials [14, 24]. In contrast, the molecular structure of 9HL is similar to the structure of typical conventional smectics, and nano-segregation of such molecules seems to be less probable. The reasons for the de Vries-type behaviour observed in 9HL were thus not clear, motivating a detailed study of the order parameters using different techniques in order to clarify the properties of 9HL.

In particular, valuable information about the molecular orientational distribution in de Vries-type materials can be found by determining the higher order parameter $<P_4>$, which may be used to distinguish between a conventional and a de Vries scenario of the SmA–SmC (SmA*–SmC*) phase transition [17]. In other words, a de Vries-type scenario could be well described by either a "volcano-like" (negative $<P_4>$) or a "sugar loaf" (high OOP) distribution function. Therefore, 9HL appears to be an exceptional candidate for experimental study in order to gain insight into the nature of the so called de Vries-type behaviour.

In this work we use both polarized Raman spectroscopy and x-ray scattering to determine the $<P_2>$ and $<P_4>$ in the smectic liquid crystal 9HL. In the SmA* phase, the parameter $<P_2>$ is also estimated from measurements of the refractive indices. In addition, the smectic order parameter Σ is obtained from x-ray experiments. DFT molecular modeling of the 9HL was used to calculate both its Raman spectrum and its molecular structure. The temperature variation of the order parameters is discussed in terms of the Maier-Saupe mean-field theory. Finally, we use the results of x-ray and viscosity measurements to prove the existence of a more ordered phase exhibited by this material at lower temperatures, most likely the SmF* phase.

The paper is arranged as follows: Some results of the general theory of polarized Raman spectroscopy are discussed in section II. Section III contains a discussion of the basic ideas used to determine the order parameters from the x-ray measurements. The experimental details are described in section IV. Section V contains a detailed discussion of the order parameters obtained using the methods described in sections II and III. Finally, the conclusions of the work are presented in section VI. Additional information concerning refractive indices, Raman depolarization ratio as well as the SmF* phase are presented in the appendices.

II. POLARIZED RAMAN SPECTROSCOPY

Raman scattering is an inelastic scattering process that arises as a result of the interaction of light with the derivatives of the second rank polarizability tensor α_{ij}, with respect to the distortion coordinate Q_k in a physical medium. In general, the Raman intensity as measured in the laboratory frame XYZ, $I \propto (\partial_{Q_k}\alpha_{ij})^2 \equiv (\alpha_{ij}')^2$, can be calculated in terms of the components of the diagonal polarizability tensor defined in the local molecular frame $x'y'z'$ [26]. Therefore, information about the local molecular order with respect to the laboratory frame can be extracted analysing the Raman signals. In particular, Jen *et al.* laid the foundations of

the polarized Raman spectroscopy in liquid crystals [5]. In this method the order parameters $<P_2>_R$ and $<P_4>_R$ can be determined from the depolarization ratios of two different aligned samples. In recent years Hayashi *et al.* have presented a more general vision of the PRS technique [22, 23, 32-34]. It has been shown that better results could be achieved if one takes into account the whole polarization angle dependence of the depolarization ratio obtained from the Raman signal. Additionally, corrections from refractive and birefringence effects are included in their theoretical model. Even corrections from distortions in the pitch can in principle be taken into account in the analysis. A similar approximation to extract the OOP from the Raman intensity was introduced by Jones *et al.* [35]. The performance of these two Raman methods is discussed in the appendices section.

The Raman intensity signal contains information about a fourth rank orientational ordering tensor and, consequently, the fourth order moments of the orientational distribution function $f(\beta, \alpha, \gamma)$ can also be determined. As shown by van Gurp and Zannoni *et al.* [2, 9, 36], symmetry arguments can be applied to the elements of $f(\beta, \alpha, \gamma)$ and, in particular, for a liquid crystal medium some simplification can be accomplished. As a matter of fact, specific uniaxial Raman vibrations of the molecule can in principle fulfil these requirements. Under these conditions, the distribution function can be expanded to fourth order using Wigner functions. In particular, for the uniaxial Raman vibration, i.e. $\gamma = 0$, one obtains:

$$f(\alpha,\beta)=\frac{1}{8\pi^2}(1+\frac{5}{2}<P_{200}>_R P_2(\beta)+\frac{9}{8}<P_{400}>_R P_4(\beta)+\frac{30}{2}<P_{220}>_R (1-\cos^2\beta)\cos2\alpha$$
$$+\frac{540}{8}<P_{420}>_R (8\cos^2\beta-7\cos^4\beta-1)\cos2\alpha+\frac{630}{8}<P_{440}>_R (1-2\cos^2\beta+\cos^4\beta)\cos4\alpha) \tag{1}$$

Here, P_2 and P_4 are the Legendre polynomials and $<P_{200}>_R$ and $<P_{400}>_R$ represent the uniaxial nematic order parameters. The biaxial OOP $<P_{220}>_R$, $<P_{420}>_R$ and $<P_{440}>_R$ describe the biaxial distribution of long molecular axes which may be present, for instance, in tilted smectic phases. Therefore, the polarized Raman spectroscopy can be applied to either uniaxial or biaxial phases provided the active Raman vibration is uniaxial and well defined. Recently this method has been used by Southern *et al.* to determine a number of biaxial order parameters in the biaxial nematic phase [37].

In general terms, the Raman intensity profile I_{ij} measured in the laboratory frame as a function of the orientation ω can be expressed in terms of the derivative polarizability tensor α_{ij}' of a particular Raman vibration. The Raman response also depends on the orientation of the molecules in an element of volume V and consequently in the distribution function $f(\beta, \alpha)$. Thus, a general relationship between I_{ij}, $f(\beta, \alpha)$ and α_{ij}' can be expressed as [32];

$$I_{ij}(\omega) = I_0 \int_0^h \iint_{\alpha,\beta} \left| \alpha'(\alpha,\beta,X;\omega) \right|^2 f(\alpha,\beta) d\alpha d\beta dX \tag{2}$$

Here I_0 is the intensity of the incoming beam and the subscripts i,j denote that the sample is placed between crossed ($i \neq j$) or parallel ($i = j$) polarizers. In a planar oriented sample, ω is the angle between the symmetry axis of α_{ij}' and the polarization direction of a linearly polarized beam. The thickness of the oriented cell is denoted by h and X represents its integration variable.

When the full angular dependence ($\omega \rightarrow$ 0 - 360°) of the Raman signal is recorded, the OOP can finally be determined from the depolarization ratio D_P,

$$D_P = \frac{I_{yz}(\omega)}{I_{zz}(\omega)}$$

(3)

The expression for D_P is a function of ω and depends on a number of known parameters including, the principal refractive indices n_z, n_x as well as the refractive index of the glass plate n_g. Thus, the uniaxial and biaxial order parameters can be determined by fitting the curves using a chi-squared minimization procedure. The general mathematical form of D_P is discussed in appendix A.

III. X-RAY SCATTERING DIFFRACTION

When a collimated x-ray wave front interacts with a set of LC molecules distributed in the space *xyz* (with orientations characterised by the distribution function $f(\beta)$), the interference of the scattered waves in the forward direction yields a diffraction pattern. Since the intensity distribution $I(q_x,q_z)$ obtained from this pattern represents the Fourier transform of the pair correlation function, information about the molecular ordering can be obtained in this way [38] (see Fig. 2). Indeed, Leadbetter and Norris established for the first time the relation between the intensity profile $I(\chi)$ around the wide-angle arc of diffuse x-ray scattering and $f(\beta)$ for nematic and smectic A liquid crystals composed of uniaxial molecules [3]. Likewise, they found that information about the translational order, which is observed in all liquid crystalline smectic phases, can be extracted from the integrated intensity of the first Bragg reflection. This reflection is generated from the sequence of ordered layers in the smectic phase and is observed along the meridian q_z of the diffraction pattern as shown in Fig. 2.
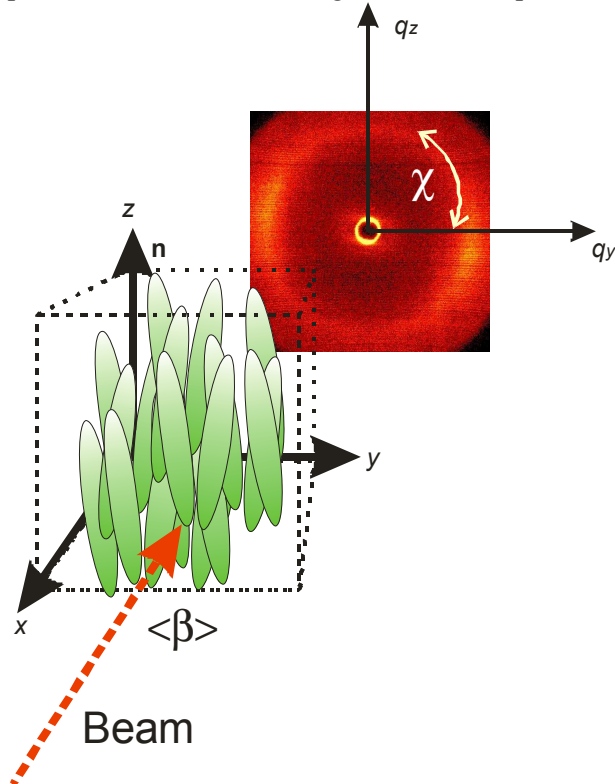
FIG. 2 (Color online) Intensity diffraction pattern generated by x-rays scattered by a set of molecules in a volume V. The fundamental Bragg reflection is observed in the inner part of the diffraction pattern. The wide-angle arc χ is also shown.

Following the ideas of Leadbetter and Norris, Davidson *et al.* [4] proposed a simple method of evaluating $f(\beta)$ from $I(\chi)$. If one expands the ODF in terms of $\cos^{2n}\beta$ functions instead of Legendre polynomials, one obtains the following expression:

$$f(\beta) = \sum_{n=0}^{\infty} f_{2n} \cos^{2n}\beta \tag{4}$$

Now it is possible to establish a simple relationship between the coefficients of the ODF and the scattering profile $I(\chi)$ using the Fourier expansion:

$$I(\chi) = \sum_{n=0}^{\infty} f_{2n} \frac{2^n n!}{(2n+1)!!} \cos^{2n}\chi \tag{5}$$

Hence, the ODF can be calculated by inserting the fitted values of the coefficients f_{2n} into equation (4), and the OOP can readily be found as the corresponding moments of $f(\beta)$ using the following equations:

$$\langle X \rangle = \frac{\int_0^{\pi/2} X f(\beta) \sin(\beta) d\beta}{\int_0^{\pi/2} f(\beta) \sin(\beta) d\beta}; \quad X = P_2 \text{ or } P_4 \tag{6}$$

On the other hand, as shown by Leadbetter *et al.*, the smectic order parameter Σ at a particular temperature T can be obtained from the x-ray scattering intensity as follows:

$$\Sigma = \frac{I(T)}{I_0} \tag{7}$$

where $I(T)$ is the integrated intensity of the first Bragg reflection at temperature T and I_0 represents the signal obtained from the same reflection in the perfectly ordered smectic structure. Kapernaum and Giesselmann recently proposed a simple method of calculating Σ [39]. In this method, the intensity I_0 is determined by using an extrapolation procedure similar to the Haller´s method of extrapolation to zero temperatures used to determine the order parameter $<P_2>$. Thus, a fitting procedure based on the temperature dependence of $I(T)$ provides the information required to estimate the smectic order parameter Σ.

IV. EXPERIMENT

We have carried out Raman, x-ray and electro-optic experiments, and different samples have been prepared for each particular method. For Raman studies, a liquid crystalline sample made of fused silica plates and rubbed with nylon has been prepared. This cell, with 1.6 μm spacers, was prepared for planar alignment of the liquid crystal. Another sample with homeotropic alignment and 20 μm spacers was used to measure the refractive indices of 9HL. For the electro-optic experiments a 1.6 μm planar-oriented sample was used. The planar

7

oriented 1.6 μm samples are rubbed in only one plate. In the x-ray case, 9HL was filled into a Mark capillary tube with the diameter of 0.7 mm.

The backscattered Raman signal of 9HL was measured using the Horiba Jobin Yvon confocal Raman spectrometer HR-800. The setup is equipped with a 634 nm linearly polarized He-Ne laser operating at 10 mW and a CCD camera is used to detect the Raman signal. The objective of the microscope (50X) focuses the laser beam into the sample in a spot around 6 μm and it is focused in a rather well aligned area of the sample. The Raman signal was measured in the two specific polarization states of the linearly polarized incoming (I_i) and outgoing (I_s) beams. In the first state, denoted I_{zz}, the linear polarizations of the incoming and outgoing beams are parallel. In the second state, denoted I_{yz}, the polarizations states are orthogonal. The sample is placed between these polarizers inside a rotatable hot stage (Linkam). The angle (ω) and temperature (T) dependence of the Raman signal with respect to the layer normal **k** is then obtained. The temperature accuracy is ± 0.1 °C.
The spectra were recorded every 10° ± 1° until a 360° full rotation of the hot stage was accomplished. The integrated intensity $I_{ij}(\omega)$, corresponding to the stretching mode of the phenyl rings, was obtained from the experimental Raman spectrum.

The x-ray scattering measurements were carried out with a Bruker NanoStar diffractometer equipped with a Göbel mirror which collimates the Cu K_α radiation. The capillary sample was mounted in a temperature controlled brass block and kept in a 1 T horizontal magnetic field. A 2D diffraction pattern was then recorded using a HiStar area detector. Finally, the intensity profiles of the diffraction pattern were extracted using the SAXS software from Bruker. The temperature controller system has a resolution of ± 0.1 °C.

Measurements of the refractive indices of 9HL are presented in appendix C.

V. RESULTS AND DISSCUSION

A. Molecular modelling

The theoretical Raman tensors of 9HL were calculated with the help of *GAUSSIAN 98* package [40], using density functional theory (B3LYP [41]) and a 6-31G* basis set. Both the calculated and the experimental spectra are shown in Fig. 3. Note that the frequencies shown in Fig. 3, corresponding to the calculated spectrum, have been scaled by a factor of $F = 0.98$ in order to achieve a good agreement in the positions of the Raman bands between the experimental and the calculated Raman spectra of 9HL. This standard scaling procedure is well described in reference [42].
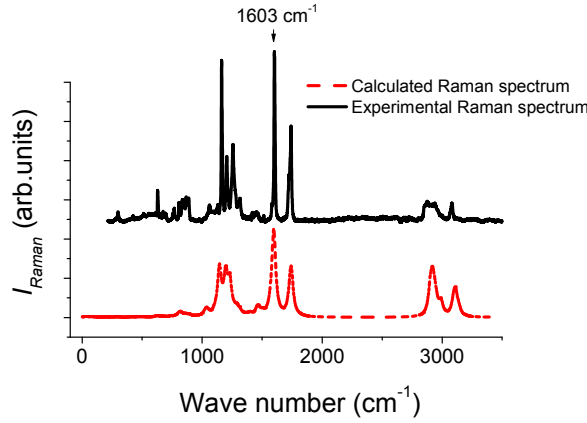
FIG. 3 (Color online) Experimental and calculated spectra of 9HL. The uniaxial Raman vibration due to the stretching modes of the phenyl rings at 1603 cm^{-1} is shown. Note that both the main active Raman bands and the relative intensities are reasonably well predicted by the calculation.

The calculation shows that the strongest Raman band observed in the experimental spectrum (1603 cm^{-1}) corresponds mostly to the uniaxial vibration of the three phenyl rings of the molecule. The directions of these vibrations as well as the principal inertial axes I_Z and I_X of the particular molecular conformation used in the calculations are depicted in Fig. 4. The inertial axis I_Y is perpendicular to I_X and I_Z. The average direction V_R of these three coupled stretching vibrations is indeed parallel to the long inertia axis I_Z.
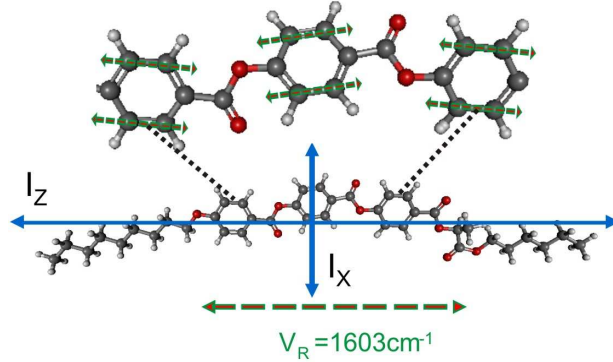

FIG. 4 (Color online) Directions of the stretching modes of the phenyl rings at 1603 cm^{-1} (green dashed arrows). The principal inertia axes I_Z and I_X of the molecule are the blue solid lines. The average direction of this Raman vibration V_R (red dash arrow) is parallel to the inertia axis I_Z. The length of the molecular conformation is approximately $L_M = 41.9$ Å.

B. Order parameter $<P_2>_R$ and $<P_4>_R$ from polarized Raman spectroscopy

The Raman signal for the particular vibration discussed above has been obtained for a planar oriented cell. Firstly the Raman intensity I_{zz} and I_{yz} is measured using two different polarization geometries. Thereafter, the full angular dependence of the depolarization ratio $D_p = I_{yz}(\omega)/I_{zz}(\omega)$ with respect to the layer normal is obtained. Fig. 5 shows the different D_p profiles observed at different temperatures and phases of 9HL. In particular, one notes two important variations of these profiles. First, a rotation of the D_p profile in the SmC* phase with respect to **k** is observed, and secondly a change of shape of the D_p profile occurs with decreasing temperature in the SmC* phase. The first variation corresponds to a change in the direction of the Raman uniaxial scattering tensor which is also accompanied by shift in frequency from 1603 cm^{-1} to 1603.5 cm^{-1} of its Raman vibration. This experimental evidence

9

suggests that the second order SmA*–SmC* transition in 9HL is accompanied by an almost unnoticeably change in its average molecular conformation. This indicates that the mean field the molecules feel is slightly different in the SmA* and SmC* phases.
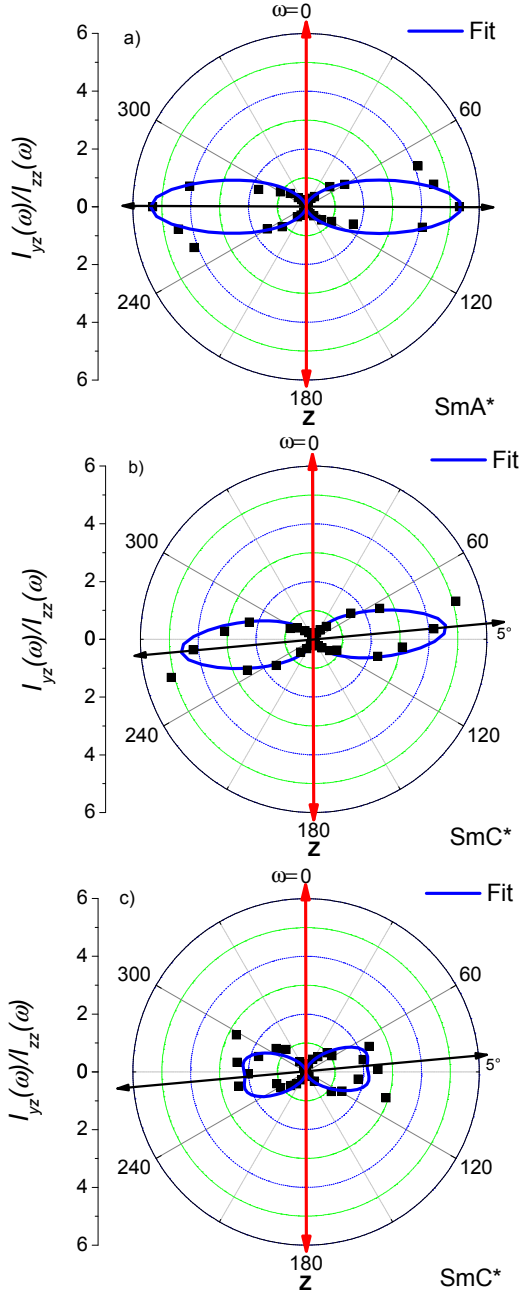

FIG. 5 (Color online) Angular dependence of the depolarization ratio $I_{yz}(\omega)/I_{zz}(\omega)$ in the SmA* a) $T =$ 100 °C and SmC* phases b) $T = 72.5$ °C, c) $T = 65$ °C. The thickness of the cell is 1.6 μm. The solid lines (blue) represent the fitted curves after a chi squared procedure according to equations (A1). Note that the depolarization ratio profile (1603 cm^{-1}) rotates 5° with respect to the layer normal **k** (red line connecting 0° and 180°) after the SmA*–SmC* transition occurs.

The second variation is related to the appearance of chevron defects in the SmC* phase. These chevron defects appears at $T = 67$ °C $i.e.$ 8 °C below the SmA*–SmC* transition. In Fig. 6 the textures, which are observed in the SSFLC cell of 1.6 μm placed between crossed

10

polarizers, are presented. In the left hand part of the cell one can distinguish the electrodes, and here the triangular wave electric field with the frequency of 270 Hz and voltage V_{pp}= 4 V is applied. In the right hand part of the cell no field is applied, and there one can follow the SmA*–SmC* transition (Fig. 6 a)→b)) accompanied by the appearance of clear ferroelectric domains. A possibly SmA*-SmC$_\alpha$* transition [30] can be immediately discarded since the current response in the electric measurements, at high and low frequencies and under different applied voltages, showed a clear single ferroelectric peak in the entire SmC* phase. At lower temperatures in the SmC* phase (Fig. 6 c)), chevron defects are observed. It is worth noting that at higher temperatures in the SmC* phase (between 67 °C and 75 °C) one never observes these chevrons, either on cooling or on heating.
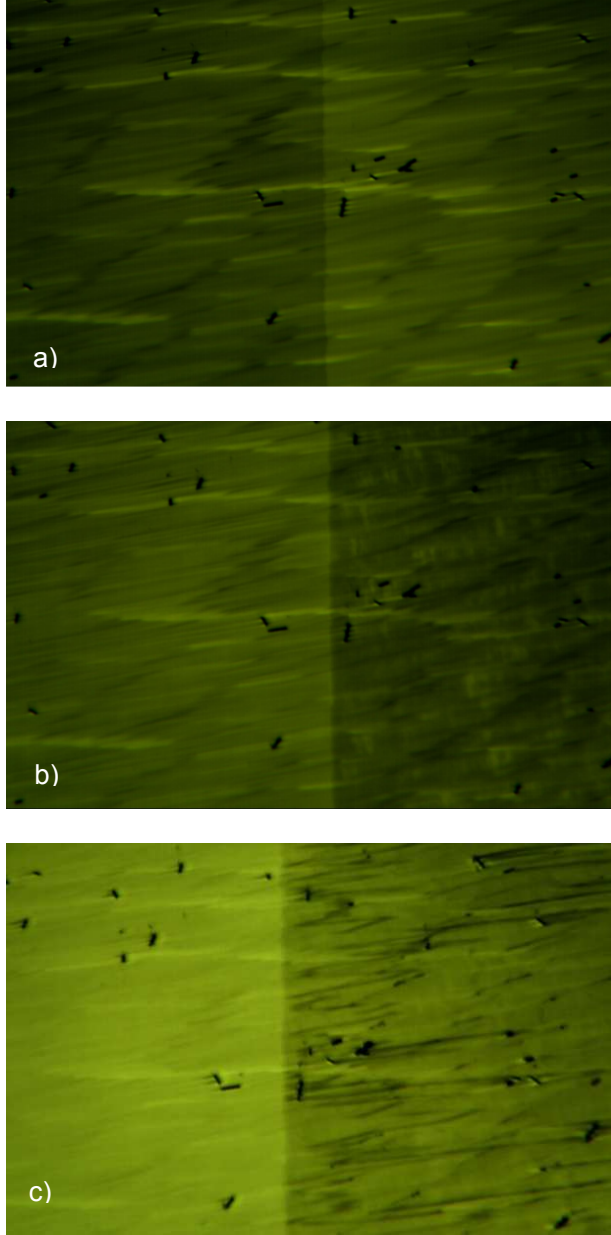

a)

b)

c)

FIG. 6 (Color online) Textures of 9HL in a SSFLC cell (1.6 µm) between crossed polarizers. In the left hand part of each picture the texture under an applied electric field, while in the right hand part the texture without an applied electric field are shown. The texture under the applied field does not change

significantly with the decreasing temperature from the a) SmA* ($T = 80$ °C) to the b) SmC* ($T = 74$ °C) phase. At the same time, the difference in textures is obvious in the part of the cell without applied field. The appearance of chevron defects in the SmC* ($T = 64$ °C) phase are clearly seen in c).

The full depolarization ratio D_p profile contains sufficient information to determine the OOP $<P_2>_R$ and $<P_4>_R$ in the SmA* and SmC* phases. Following the method proposed by Hayashi *et al.* [32], one can calculate these order parameters provided the refractive indices are known.

According to the requirements of the theoretical model, we have measured both $D_p = 0.47$ in the isotropic phase ($V_R = 1603$ cm^{-1} at $T = 136$ °C) and the principal refractive indices n_o and n_e in the smectic phases. The values of n_o and n_e can be used to correct the experimental data taking into consideration the effects of refraction. Inclusion of these terms in the theoretical model used to determine $<P_2>_R$ and $<P_4>_R$ improves the reliability of the results substantially. The refractive index of the glass was taken as $n_g = 1.515$. Using these values one can simultaneously determine $<P_2>_R$ and $<P_4>_R$ for a particular temperature T. The D_p fitted curves after fitting according to the equation (A1) are shown in Fig. 5. In appendix D we present experimental evidence of the existence of the intermediate SmF* phase between the SmC* and crystalline phases shown in Fig. 7. Note that the OOP in the SmC* phase are measured with respect to the layer normal **k**; nevertheless, the value of $<P_2>_R$ with respect to **n** could be determined after taking into account the optical tilt angle θ [23]. The temperature variation of the uniaxial orientational order parameters in different phases of 9HL is depicted in Fig. 7.
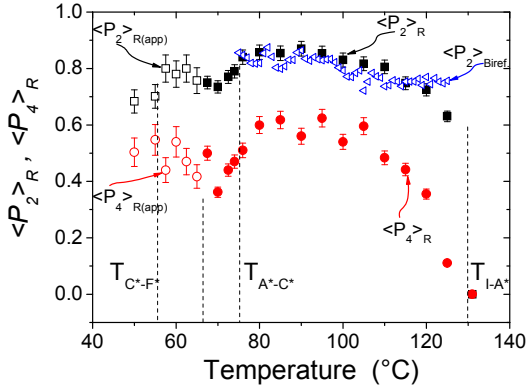

FIG. 7 (Color online) Uniaxial orientational order parameters calculated from the Raman data for 9HL. The open dots and squares represent "apparent values" of the order parameters.

The OOP determined in the SmF* phase as well as in the SmC* phase with chevron defects are calculated using Eq. (A1). It is worth noting that the model used here to determine the order parameters does not include corrections for chevron defects and its validity in the SmF* phase, where short-range bond correlations are present, is questionable. Nevertheless, these calculated values correspond to a reasonable behaviour of the OOP at the SmC*–SmF* transition. In addition, since the spot of the focused laser beam is around 6 µm, one can focus this beam into a well-oriented region between the lines forming the chevron defects. This reduces the experimental error introduced when domains with different orientations are probed simultaneously during the experiment. In any case, due to these approximations the OOP must be denoted as "apparent values" as indicated in Fig. 7.

Additionally, we have measured the birefringence of 9HL in the SmA* phase using the interference method described in ref. [43]. We then applied the extrapolation method

12

described in ref [44, 45] to calculate the order parameter $<P_2>_{Biref}$ from the birefringence data. The cell used in this experiment has a thickness of 1.6 μm. The temperature variation of $<P_2>_{Biref}$ in the SmA* phase is depicted in Fig. 7. Since that parameter is measured for the core part of the molecules in the Raman experiments, one should expect approximately the same result from the birefringence data. Indeed, one notes a good agreement between the values of $<P_2>_{Biref}$ and $<P_2>_R$ presented in Fig. 7.

The influence of the optical power of the laser in the determination of the OOP has also been taken into account. Recent measurements of the OOP using PRS and carried out in nematic materials have yielded a strong dependence of $<P_2>_R$ and $<P_4>_R$ on the power of the probe laser [7]. However, in the case of the material 9HL which does not posses a nematic phase, we did not find such a strong dependence. In particular, $<P_2>_R$ and $<P_4>_R$ were determined in the SmA* phase at temperature $T = 110$ °C using optical powers of 20 mW, 10 mW and 2 mW, respectively. The calculated $<P_2>_R$ and $<P_4>_R$ values do not change significantly with the increasing laser power. A maximum deviation of ± 0.05 has actually been found in the value of these order parameters. Therefore, the optical power used during the experiments did not influence dramatically the values of $<P_2>_R$ and $<P_4>_R$ in the smectic phases of 9HL.

Finally, one has to find out if any significant degree of biaxiality is present in the SmA* phase, since the values of $<P_2>_R$ and $<P_4>_R$ are obtained assuming uniaxial symmetry. For this purpose, the uniaxial OOP have been determined taking into account the terms proportional to the biaxial order parameters in the distribution function (Eq. (1)). With the help of Eq. (A1) one can also determine the biaxial order parameters $<P_{220}>_R$, $<P_{420}>_R$ and $<P_{440}>_R$ from the experimental depolarization ratio D_p. A minimization procedure enables one also to find this set of order parameters. A similar procedure has been previously successfully used by Southern *et al.* [37] to obtain the biaxial order parameters using PRS. Here, we also take into account the influence of the refractive indices in the theoretical model (see Eq. (A1). For the uniaxial phases we have assumed $<P_{220}>_R = <P_{420}>_R = <P_{440}>_R = 0$ in Eq. (A1) and therefore $<P_{400}>_R = <P_4>_R$ and $<P_{200}>_R = <P_2>_R$. Some of these results are presented in Table I.

	T (°C)	Uniaxial OOP		Biaxial OOP				
		$<P_2>_R$	$<P_4>_R$	$<P_{200}>_R$	$<P_{400}>_R$	$<P_{220}>_R$	$<P_{420}>_R$	$<P_{440}>_R$
SmA*	125	0.63±0.02	0.12±0.04	0.63±0.04	0.11±0.08	$<10^{-3} \approx 0$	$<10^{-3} \approx 0$	$<10^{-3} \approx 0$
	100	0.83±0.02	0.54±0.04	0.83±0.04	0.60±0.08	$<10^{-3} \approx 0$	$<10^{-3} \approx 0$	$<10^{-3} \approx 0$
SmC*	85	0.85±0.02	0.61±0.04	0.85±0.04	0.55±0.08	$<10^{-2}$	$<10^{-2}$	$<10^{-2}$
	72	0.77± 0.02	0.44±0.04	0.76±0.04	0.43±0.08	$<10^{-2}$	$<10^{-2}$	$<10^{-2}$
	60	0.78± 0.02	0.54±0.04	0.74±0.04	0.45±0.08	$<10^{-2}$	$<10^{-2}$	$<10^{-2}$

TABLE I Values of the uniaxial and biaxial orientational order parameters at temperatures; $T = 125$, 100 and 85 °C (SmA*), $T = 72$ and 60 °C (SmC*). This set of order parameters has been calculated using Eq. (A1). The thickness of the sample is 1.6 μm.

The uniaxial order parameters $<P_2>_R$ and $<P_4>_R$ do not change significantly when one accounts for biaxial ordering in 9HL. Actually, the biaxial order parameters found in the SmA* phase are very small and the experimental uncertainties are much bigger than $<P_{220}>_R$, $<P_{420}>_R$ and $<P_{440}>_R$ in some cases. Thus, one may safely neglect any biaxiality in the SmA* phase which is consistent with its generally accepted uniaxial symmetry. In the SmC* phase, which is generally biaxial, we indeed observe a small increase in the values of the biaxial terms, but they are still too low in comparison with those reported in the nematic biaxial phase

13

(see ref. [37]). Therefore the uniaxial OOP obtained here for 9HL (actually for the core part of the molecule) are not significantly affected by any biaxiality. This is in contrast to smectic de Vries materials where biaxiality has been reported to play an important role [22].

C. Order parameters from x-ray scattering diffraction

In a second set of experiments, the OOP in the SmA* as well as the apparent OOP in the SmC* phase have been determined by means of x-ray scattering experiments. The general procedure to obtain the OOP from these experimental data is described elsewhere [3, 4, 24] and the experimental details of these measurements are described in our previous publication [7]. Characteristic scattering diffraction patterns in the SmA* and SmC* phases of 9HL are depicted in Fig. 8.
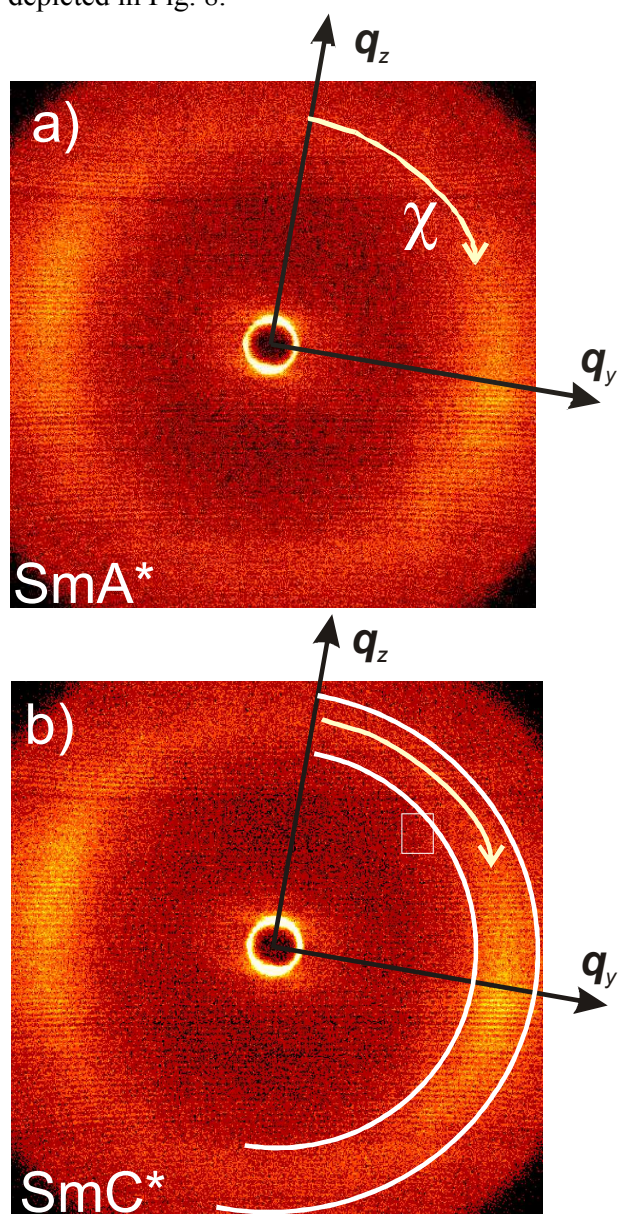
FIG. 8 (Color online) 2D-diffraction patterns of 9HL aligned by a vertical magnetic field at a) $T = 100$ °C and b) 68 °C. The wave vector $\mathbf{q}_z$ is parallel to the layer normal $\mathbf{k}$. The angular distribution is obtained from the intensity profile $I(\chi)$.

The intensity profiles $I(\chi)$ around the wide-angle (WAXS) arc χ are shown in Fig. 9. They are obtained, by integrating for each particular χ along $|\mathbf{q}|$, in the region limited by the two white rings shown in Fig. 8. The function $I(\chi)$ is then fitted using equation (4) and $<P_2>_X$ and $<P_4>_X$ are directly determined from equations (5) and (6) following Leadbetter's model [3].
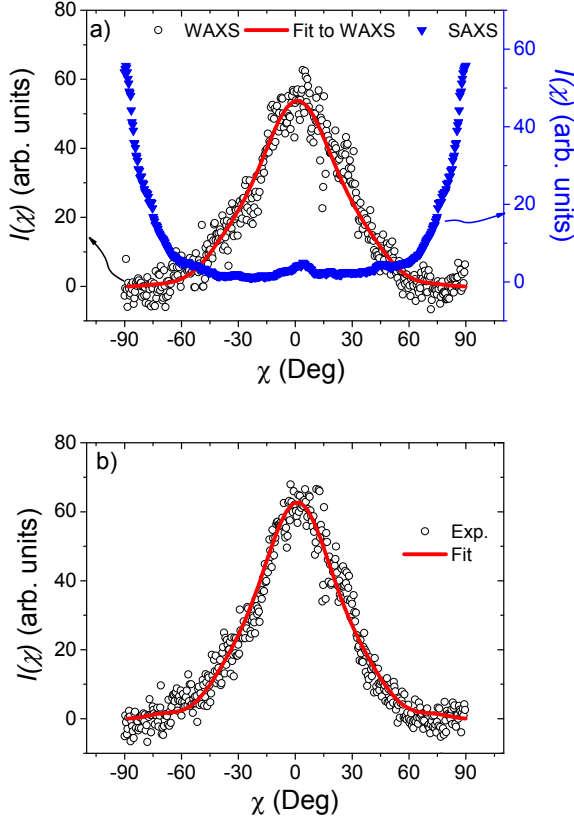

FIG. 9 (Color online) Scattering profile $I(\chi)$ measured in the a) SmA* ($T = 100$ °C) and b) SmC* ($T = 68$ °C) phases of 9HL. The continuous red line represents the fit from equation (5) and the blue triangles trace the small angle x-ray scattering (SAXS).

One notes immediately that the shape and orientation of the diffraction pattern observed in the SmA* phase are the same as that in the SmC* phase (see Fig. 8). As long as the system cools down from the SmA* to the SmC* phase one only observes a gradual increase of the intensity around $\chi = 0$ (around the $\mathbf{q}_y$ axis in Fig. 8) of the diffuse rings in the wide arc-angle. This must correspond to a gradual increase in the orientational order parameters. Apart from this, neither a broadening of the WAXS signal nor a splitting of the SAXS signal, usually observed in conventional smectics, has been detected at the transition. This peculiar behaviour has already been reported by Lagerwall *et al.,* in a chiral de Vries-type material and is in contrast with what is observed in conventional smectics [24].

Since the diffraction patterns in the SmA* and SmC* phases are rather similar and because the tilt angle of 9HL is relatively small ($\approx 16°$), we calculated the order parameter in the SmC* phase using the same uniaxial approximation as in the SmA* phase. Nevertheless, these parameters are denoted as apparent values in this context and can be used only as a first

15

approximation. The OOP in the SmA* and SmC* phases determined using the x-ray experimental data are presented in Fig. 10.
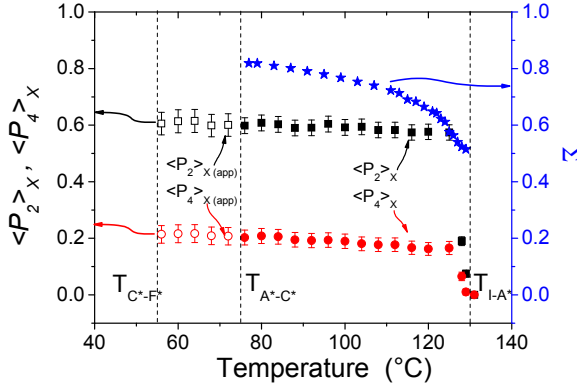

FIG. 10 (Color online) Orientational order parameters $<P_2>_X$ (squares) and $<P_4>_X$ (dots) obtained from x-ray experimental data for 9HL. The open dots and squares represent apparent values of the order parameters. The translational order parameter Σ (stars) in the SmA* phase is also shown.

The values of the order parameters obtained from x-ray scattering may be influenced by the formation of small molecular clusters which are differently oriented in space *i.e.,* by a possible mosaicity of the phase [46, 47]. This could degrade the quality of the x-ray signal in the wide angle measurements and consequently the values of $<P_2>_X$ and $<P_4>_X$ could be underestimated. SAXS measurements provide information about the formation of the layers in the smectic phases, with the behaviour of the SAXS along the arc χ related to the orientation and order of the layers in space. Indeed, perfect layering in the SmA* phase corresponds to two narrow peaks centered at $\chi = -90°$ and $\chi = 90°$ in the SAXS. In contrast, imperfect layering or a mosaicity in the smectic phase will critically broaden those peaks. In the last case, the SAXS signal may certainly effect the WAXS signal, and as a consequence the values of the OOP may be incorrect. In other words, the WAXS and SAXS signals may, to a certain extend, be convolved along χ. The SAXS signal, re-scaled to the WAXS signal and integrated along χ, is depicted in Fig. 9. In order to compare both signals it has been necessary to rescale the SAXS signal which is approximately 50 times stronger than the WAXS signal.
In the first approximation, we have estimated this effect on the evaluation of the OOP by means of a deconvolution process of the fitted WAXS signal and the SAXS signal (see Fig. 9). Then, the OOP have been calculated again from the deconvoluted WAXS signal. The results correspond to a variation of the order parameters of about + 0.04 in this case. This variation is already included in the error bars in Fig. 10, and therefore one can safely ignore this effect.

Finally, the translational smectic order parameter in the SmA* phase was determined from the integrated intensity of the first Bragg reflection [39]. The gaussian peak integrated along $\mathbf{q}_z$ in the SAXS region, which provides information about the smectic order, is the one observed as the first Bragg reflection in Fig. 8. Therefore, the OOP as well as the translational order parameter can be determined simultaneously. The results obtained for 9HL are depicted in Fig. 10. One can readily see that the smectic order is rather high at the SmA*–SmC* transition. This result supports the idea that the layers in the SmA* phase are strongly ordered and therefore the mosaicity in the phase should be small.

16

D. Orientational order parameters in the context of the Maier-Saupe theory

We now compare the experimental values of $<P_2>$ and $<P_4>$ obtained from the PRS and x-ray experiments in the uniaxial SmA*, (see Fig. 11 a)). These values are also plotted in the $(<P_2>, <P_4>)$ plane (see Fig. 11 b)) and analysed in the context of the universal Maier-Saupe mean field theory [48].
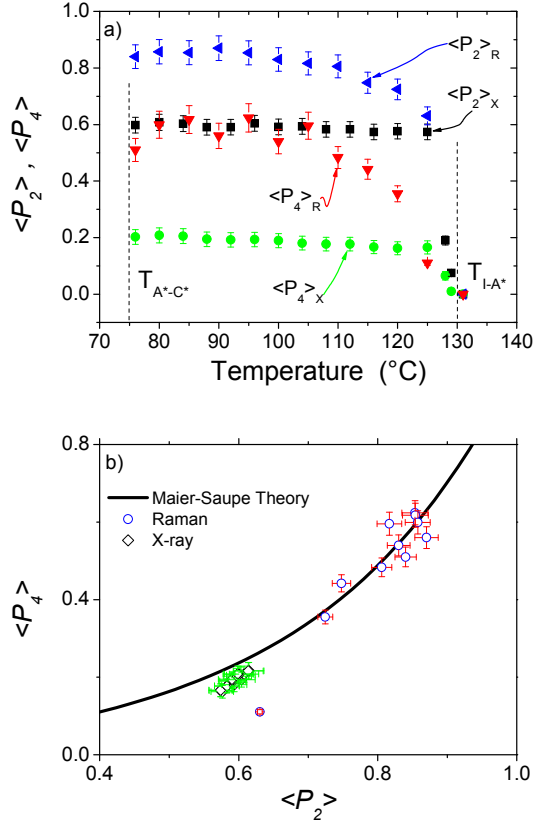

FIG. 11 (Color online) a) Comparison of the orientational order parameters measured by polarized Raman spectroscopy and x-ray scattering in the SmA* phase. b) Comparison between the experimental ratio of the order parameters determined in the SmA* phase and the theoretical curve $<P_2>$ vs. $<P_4>$ (solid curve) obtained using the Maier-Saupe mean-field theory. Note that the values of $<P_4>$ are positive in all cases.

One can readily see from either Fig. 11 a) or Fig. 11 b) that there is a large discrepancy between the raw values of OOP determined using the two different experimental techniques. In particular, the difference between the $<P_4>_R$ and $<P_4>_X$ values is very large. At the same time, a really good agreement between the experimental results and the universal Maier-Saupe curve in the $(<P_2>, <P_4>)$ plane is achieved (see Fig.10 b)). This means that the thermodynamic relationship between $<P_2>$ and $<P_4>$ is preserved and confirms that the ratio should be independent of the experimental method used to determine the order parameters.

The OOP of a particular liquid crystalline phase can be determined by probing different functional groups of the molecules. Even if one uses the same experimental method, the OOP determined for every functional group might have different values. This is because different groups may have different orientations with respect to the long molecular axis and therefore,

17

on average, with respect to the director **n**. Therefore, depending on their relative orientation, these groups may possess different degree of orientational order [5, 7, 29, 32, 49-51]. Despite these differences, one may still find a relationship between OOP for different groups by applying the coordinate transformation between their relative effective orientations in space [52]. The OOP obtained for a particular functional group are expected to follow the Maier-Saupe prediction for the ratio $<P_2>/<P_4>$ provided they are measured in a uniaxial phase.

The Raman technique provides information on the relative average orientation of a specific functional group of the molecule with respect to the layer normal **k**. In our case, the orientation of the uniaxial stretching mode of the benzene ring has been studied. This vibration is related to the orientation of the molecular core which corresponds to approximately 50% of the whole molecular volume in the case of 9HL. Then the OOP presented in Fig. 7 characterises the average orientational order of the molecular core. On the other hand, the x-rays interact with all atoms in the molecule and the OOP shown in Fig. 10, representing the average orientational order of the whole molecule, may be different from that of the molecular core. Therefore, depending on the experimental method used to determine the OOP, one might expect small differences in the values of OOP. This is because each experimental method probes features of the molecular distribution in a different way, and different methods may even probe orientational distributions of different parts of the molecule. With this in mind, we will give a possible interpretation of the discrepancies in the values of OOP obtained by the two experimental techniques (see Fig. 11 a)) in the next section.

E. Comparison of the orientational order parameters obtained by Raman and XRD.

In this section, we discuss the discrepancies in the values of the OOP shown in Fig. 11 a) in terms of the molecular structure of 9HL. The x-rays interacting with the atoms of 9HL have a perspective of the molecule similar to that depicted in Fig. 12. Here, each atom of the molecule is represented by a sphere with an associated partial charge.
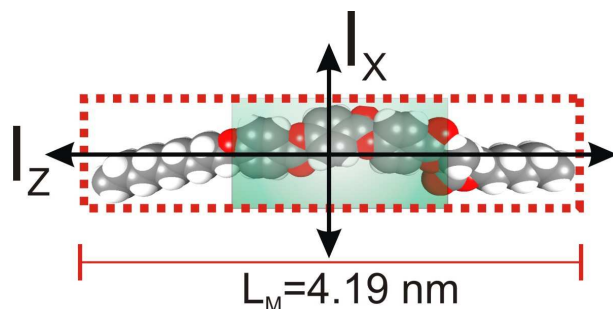

FIG. 12 (Color online) Atomic molecular conformation of 9HL according to the DFT calculations, see VII A. The principal inertia axes I_Z and I_X of the molecule are represented by the solid lines. The dotted box approximately presents the surface of the averaged, rigid rod-like structure of the molecule which is generated when the molecule rotates around its inertia axis I_Z.

The interference of the scattered x-ray waves from atoms in a given molecule and from a large number of molecules in the sample yields the diffraction pattern presented in Fig. 8. The hydrogen atoms are practically transparent to the x-ray wave. Note that around 70 % of the atoms in the molecular structure of Fig. 12 are located around the core. This indicates that the major contribution to the diffraction patterns observed in the WAXS region should be generated from this part of the molecule. At the same time, the contribution to the WAXS

18

signal coming from the atoms located in the alkyl chains must also be taken into account since these tails represent approximately 50 % of the length of the molecule which is visible in the x-ray spectra. The distribution of atoms in the alkyl chains, which are normally tilted with respect to the core, may also give rise to an additional specific molecular axis which should be taken into consideration in the interpretation of the x-ray data.

The interpretation of the x-ray scattering data should be based on a reasonable molecular structure of 9HL. The results of section V A and B suggest that the molecular structure presented in Fig. 4 may be a good candidate for the most probable conformation of the molecule. This model can now be tested by estimating the temperature dependent layer spacing d in the SmA* phase using the following approximate relation [24]:

$$d = L<\cos\beta> \tag{8}$$

and comparing it with the layer spacing determined experimentally from x-ray scattering data. Eq. (8) establishes a simple relationship between the smectic layer spacing and the average projection of the molecule of length L on the layer normal $\mathbf{k}$. Here β is the angle between the molecular long axes and the director which is parallel to $\mathbf{k}$. Using the molecular model presented in Fig. 3 one obtains $L=L_M = 4.19$ nm. The average $<\cos\beta>$ is then calculated using the OOP obtained from the Raman scattering data which are presented in Fig. 11 a).

The temperature variation of the layer spacing calculated using Eq. (8) is presented in Fig. 12 together with experimental values of layer spacing d for 9HL obtained in the previous SAXS experiments [12]. One can readily see that the calculated layer spacing d_{Raman} is in good agreement with the experimental spacing d_{SAXS} at all temperatures in the SmA* phase which supports the validity of the molecular model.
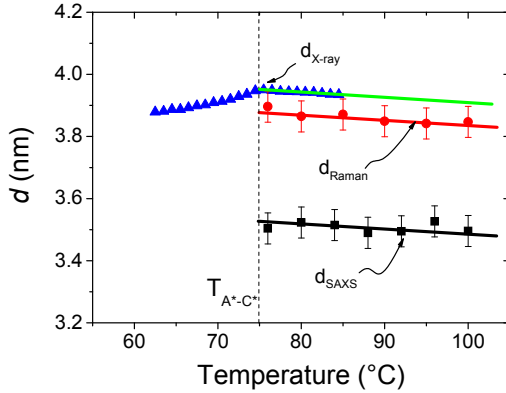

FIG. 13 (Color online) Temperature variation of the layer spacing calculated using Eq. (8) and the OOP obtained from Raman and x-ray data in the SmA* phase. The molecular length is L_M=4.19 nm. The layer spacing obtained from the position of the fundamental Bragg reflection in the SAXS experiments of ref. [12] is also presented.

On the other hand, the average $<\cos\beta>$ can also be calculated using the OOP obtained from x-ray scattering data presented in Fig. 11 a). Using the same molecular length $L=L_M = 4.19$ nm one obtains much smaller layer spacing as shown in Fig. 13 (lower curve). A good agreement between the calculated and the experimental values of the layer spacing can be achieved if a larger value of the effective molecular length ($L=L_V = 4.55$) is used in Eq. (8).

19

However, even if one manipulates and elongates the molecular model presented in Fig. 12, the maximum possible molecular length appears to be about $L_M^{(max)} = 4.4$ nm, *i.e.* smaller than L_V. This contradiction may be interpreted in the following way.

It is reasonable to assume that the x-ray scattering intensity is determined by some effective "molecular" length which may be larger than the actual length of the isolated molecule due to the effects of strong, short-range intermolecular correlations. Indeed, the x-ray scattering intensity is essentially the integral of the Fourier transform of the two-particle distribution function and thus it cannot be reduced to a one-particle property. This interpretation is consistent with the original Leadbetter model [3, 4] used to derive Eq. (5). As discussed by Leadbetter, the orientational distribution function in Eq. (5) and (6) characterises the properties of a group of neighboring molecules which are linked by strong short-range orientational and positional correlations.

One may also assume that the long axis of the correlated molecular "cluster" can be tilted with respect to the long axis of an individual molecule even if the molecules are approximately parallel within the "cluster". This is schematically illustrated by a simple example of a "dimer" shown in Fig. 14, where we assume that the most probable configuration of the two neighbouring uniaxial molecules is shown.
In this configuration the long axes of the molecules are parallel but one molecule is shifted with respect to the other along the long axis. The primary inertia axis of this molecular pair is consequently tilted with respect to the molecular axis by the angle η, and the length L_V of the pair in this direction is larger than the molecular length. If the corresponding peak of the two-particle distribution function is sufficiently high, the x-ray scatteriting experiment will mainly probe the orientational distribution of such axes rather than those of individual molecules.
In real materials the short-range intermolecular correlations should be more complicated, but these unique features will be preserved. This simple example is presented here in order to demonstrate in principle how an additional microscopic axis may appear.

The appearance of the microscopic directions determined by short-range correlations may be also interpreted from the packing point of view in the context of the Leadbetter model used to obtain the OOP from the WAXS experiments. One of the main assumptions of this model is that, on average, the atoms are cylindrically distributed around the long molecular axis in order to form a surface of revolution which generates the diffraction pattern. For the 9HL molecule, one finds that the cylindrical distribution of atoms around the inertia axis I_Z creates a surface which contains too much free space inside, and this is unfavourable from both interaction energy and close-packing points of view as can be seen already in Fig. 12. Nevertheless, one can easily find at least two molecular axes which provide a much better packing after the molecules are rotated along these axes. The orientation of any of such axes, however, is different from the orientation of I_Z.
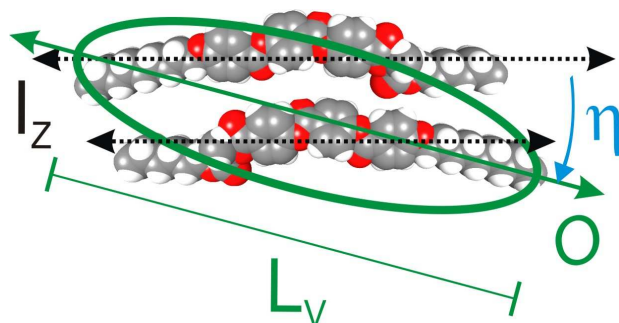
FIG. 14 (Color online) Schematic representation of a strongly correlated pair of neighbouring molecules where the long axis O of the pair is tilted by the angle $\eta \approx 23°$ with respect to the inertia axis I_Z of the individual molecules, and the length L_V of the pair along the primary axis is larger than the molecular length L_M.

Following these ideas we assume that the order parameters calculated from the x-ray scattering data characterise the orientational distribution of some microscopic axis O_i, determined by short-range correlations between the molecule i and its nearest neighbours, which makes an angle η with the long molecular axis I_Z. At the same time, as discussed in sections V A and D, the OOP calculated from the Raman scattering intensity characterize the orientational distribution of the long molecular axes. The relation between the two sets of order parameters measured independently for two different axes O_i and I_Z can be derived using the addition theorem for the Legendre polynomials as first proposed by LaFrance *et al.* [52]. Assuming that the short molecular axes are randomly distributed about the director (since the phase is uniaxial) one obtains

$$< P_n(O_i \cdot n) >=< P_n(I_Z \cdot n) > P_n(\eta), \text{ n = 2, 4} \tag{9}$$

where η is the angle between the axes, $<P_n(O_i \cdot n)>$ represent the order parameters obtained from x-ray scattering data and $<P_n(I_Z \cdot n)>$ are the order parameters derived from the Raman scattering profile.

The angle η can be estimated in the following way. As discussed above, the layer spacing in the SmA* phase can be expressed as, see Eq. (8): $d = L_V <cos\beta'>$, where $L_V = 4.55$ nm and where the average $<cos\beta'>$ is calculated using the OOP obtained from x-ray scattering intensity distribution. Extrapolating this equation to low temperatures one obtains $\beta' \approx \eta$ and $d \approx L_M$, and hence $L_M \approx L_V cos\eta$ provided the angle η is weakly temperature-dependent. Using the value of the molecular length $L_M = 4.19$ nm obtained from the molecular model (see above) one concludes that $\eta \approx 23°$.

Substituting this result into Eq. (9), one can rescale the OOP obtained by x-ray scattering and compare them with the OOP from the Raman data. One can readily see from Fig. 15 that the rescaled OOP from x-ray agree well with the OOP measured using Raman scattering, with the match between the $<P_4>$ values being particularly good. One notes also that in this rescaling procedure the angle η is not a fitting parameter but is calculated using the molecular length, the temperature-dependent layer spacing, and experimentally measured OOP as described above. Usually, introducing either scaling or empirical correction factors to match simultaneously the experimental values of $<P_2>$ or $<P_4>$ results in the correct scaling of $<P_2>$ values only [6, 53-56], with the match between different $<P_4>$ values typically much worse. The rescaling procedure described above enables us to match the values of $<P_2>$ and $<P_4>$ simultaneously and precisely, a result that supports the model presented above.
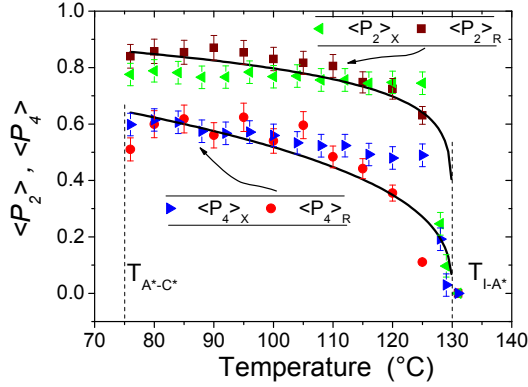
FIG. 15 (Color online) Comparison of the rescaled orientational order parameters obtained from x-ray scattering and the order parameters obtained from Raman experiments. The solid lines are curves of tendency.

VI. CONCLUSIONS

In this paper we have presented a detailed comparative study of the temperature variation of the orientational order parameters $<P_2>$ and $<P_4>$ in the SmA* and SmC* phases of 9HL using both polarized Raman spectroscopy and x-ray scattering diffraction. We have also made birefringence measurements in order to get an independent estimate of the order parameter $<P_2>$ in the SmA* phase, and obtained the smectic order parameter Σ from x-ray experimental data.

The values of the primary nematic order parameter $<P_2>_R$, obtained from the Raman experiments, are in good agreement with the values of $<P_2>_{Biref}$ obtained from birefringence measurements and also in agreement with recently published NMR results for deuterated 9HL [28]. Generally, this is what one might expect since all of these methods probe the order of the molecular core of a liquid crystal material.

The agreement between the results obtained by these three different experimental methods indicates that Raman spectroscopy provides reasonably accurate values of the OOP for this material despite some approximations involved in the interpretation of the experimental data. In particular, the general accuracy of the Raman method is mainly limited by the birefringence, which cannot be neglected when the polarization of the propagating light is not parallel to an optical axis of the anisotropic material. The particular equations used in this paper as well as in previous work [22, 23, 32-34, 37] to extract the OOP correspond to the case of thin cells where the phase shift between the ordinary and extraordinary wave is negligibly small, however, birefringence corrections may not be neglected. We have also calculated theoretical Raman tensors of the 9HL molecule using the density functional theory, and the predicted Raman spectra are in very good agreement with experiment. The molecular calculations indicate that the strongest Raman band observed in the experimental spectrum (1603 cm^{-1}) corresponds to the uniaxial vibration of the three phenyl rings of the molecule. The average direction of these three coupled stretching vibrations is indeed parallel to the long inertia axis. This band has been used in our experiments, and thus one concludes that the OOP obtained from Raman data do characterise the orientational distribution of primary molecular inertia axes.

The values of OOP obtained from x-ray scattering appear to be significantly lower than those obtained by the Raman method, with a discrepancy too big to be explained by experimental error, particularly for the order parameter $<P_4>$. This discrepancy is generally related to the fact that the distribution of the x-ray scattering intensity is not determined only by molecular cores, but depends on the orientation of the whole molecule and, in particular, on short-range intermolecular orientational correlations and packing effects.

The difference between the values of OOP obtained from Raman and x-ray experiments can be explained if one assumes that there exists an additional microscopic axis which is determined by short-range orientational and positional correlations between neighbouring molecules and which is tilted with respect to the average long axis of the individual molecules. The OOP obtained from x-ray scattering in this case characterise the orientational distribution of such "cluster" axes while the OOP obtained from Raman experiments specify the orientational distribution of long molecular axes, which explains why the OOP obtained from x-ray data appear to be smaller.

The angle between the two axes was calculated directly using the experimental smectic period, the molecular length derived from the molecular calculations and the experimentally determined order parameters. Using this angle the OOP obtained from x-ray experiments was recalculated using a general formula which establishes a relationship between the OOP for two different axes. The rescaled OOP coincide well with the values obtained from Raman data except for a small difference in the temperature variation of $<P_2>$ and $<P_4>$, which may be related to a slow variation of the angle η.

9HL exhibits a rather broad SmA* phase of about 55 °C. Thus one may intuitively expect rather high OOP at the SmA*–SmC* transition, as observed in another de Vries-type material TSiKN65 which possesses a SmA* phase of 30 °C. As shown by Hayashi *et al.* [22, 23], in TSiKN65 the order parameter increases from $<P_2> \approx 0.44$ at the I–SmA* transition to $<P_2> \approx 0.65$ at the SmA*–SmC* transition. If the SmA* phase in TSiKN65 were as broad as in 9HL, one can extrapolate their data and find the value $<P_2> \approx 0.72$ at this virtual SmA*–SmC* transition. Thus, a value of $<P_2>_R \approx 0.83$ at the SmA*–SmC* transition in 9HL is not very surprising taking into account that the SmA* phase is so broad. Recent measurements of the OOP of non-chiral de Vries-type materials, determined by means of x-ray scattering [29], found a strong difference in the $<P_2>$ values as determined for different parts of the molecules. In particular, they have found an order parameter of $<P_2> \approx 0.7$ for the hydrocarbon part of this molecule in the SmA phase which is constant over a temperature interval of 22 °C. In contrast, the value for the siloxane tails is much lower, $<P_2> \approx 0.45$. All this suggests that in some de Vries-type materials, one may find particular molecular fragments with a relatively high orientational order, even though the average order of the molecule may be low.

Following the same ideas, a relative high smectic order should be expected at the SmA*–SmC* transition in 9HL because of the broad range of the SmA* phase.
Indeed we have found a smectic order parameter $\Sigma \approx 0.82$. Event though this value is not as high as that found in other de Vries materials, it is higher than typical values found in conventional smectics [39]. In any case, one notes that some molecular fragments exhibit both high orientational and high positional order at temperatures close to the SmA*–SmC* transition in 9HL while some other fragments may be weakly orientationally ordered. The role of such individual molecular fragments in the promotion of de Vries-type behaviour is

not clear. Further experiments on similar de Vries-type materials will help to clarify this point.

Finally, we note that both experimental techniques yield strictly positive and relatively large values of the order parameter $<P_4>$. The lowest values of $<P_4>$ found in our experiments are as large as those observed in conventional smectic liquid crystals. The measurements indicate that the orientational distribution function in the smectic A* phase of 9HL is close to the conventional "sugar loaf" shape with one pronounced maximum [17]. This is also confirmed by the observed temperature variation of the ratio $<P_2>/<P_4>$, which is well described by simple Maier-Saupe theory.

ACKNOWLEDGMENTS

APPENDIX A: DEPOLARIZATION RATIO

Following the mathematical formalism introduced by Hayashi *et al.* [32, 33] in order to obtain the uniaxial OOP from PRS, we present here some more general expressions including biaxial terms. These biaxial terms vanish in the uniaxial nematic and smectic A phases according to the form of the distribution function in Eq. (1). The depolarization ratio including both uniaxial and biaxial order parameters as well as the dependence on the rotation angle ω can be expressed as (the calculations were performed with help of MATHEMATICA 5.0):

$$
\frac{I_{yz}}{I_{zz}} = \frac{\left(\begin{array}{l} \{3Ahb^2(m_1^2-m_2^2)T_z^2 T_{xx}^2\}\cos^4\omega \\ +\{-6Ab^2(m_1+m_2)T_x T_{xx}T_z T_{zz}\sin[h(m_1-m_2)] \\ +(m_1-m_2)(h(m_1+m_2)[315(T_x^2 T_{xx}^2+T_z^2 T_{zz}^2)a^2 \\ -210(ET_x^2 T_{xx}^2-2<P_{200}>T_z^2 T_{zz}^2)ab+(BT_x^2 T_{xx}^2+4FT_z^2 T_{zz}^2)b^2] \\ -2(315a^2+105Dab-2Cb^2)T_x T_{xx}T_z T_{zz}\sin[h(m_1+m_2)])\}\cos^2\omega\sin^2\omega \\ +\{3Ahb^2(m_1^2-m_2^2)T_x^2 T_{zz}^2\}\sin^4\omega \end{array}\right)}{\left(\begin{array}{l} \{(315a^2-210Eab+Bb^2)h(m_1^2-m_2^2)T_x^2 T_{xx}^2\} \\ +\{h(m_1^2-m_2^2)(315(T_x^2 T_{xx}^2+T_z^2 T_{zz}^2)a^2-210(ET_x^2 T_{xx}^2-2<P_{200}>T_z^2 T_{zz}^2)ab \\ +(-3AT_z^2 T_{xx}^2+4FT_z^2 T_{zz}^2+BT_x^2 T_{xx}^2-3AT_x^2 T_{zz}^2)b^2)\}\cos^4\omega \\ +\{-6Ab^2(m_1+m_2)T_x T_{xx}T_z T_{zz}\sin[h(m_1-m_2)]\sin^2\omega \\ +(m_1-m_2)(h(m_1+m_2)[630T_x^2 T_{xx}^2 a^2-420ET_x^2 T_{xx}^2 ab \\ +(-3AT_z^2 T_{xx}^2+2BT_x^2 T_{xx}^2-3AT_x^2 T_{zz}^2)b^2 \\ -2(315a^2+105Dab-2Cb^2)T_x T_{xx}T_z T_{zz}\sin[h(m_1+m_2)]\sin^2\omega])\}\cos^2\omega \end{array}\right)} \tag{A1}
$$

Where the coefficients in (A1) are:

$$A = (7 + 5 < P_{200} > -30 < P_{220} > -12 < P_{400} > -180 < P_{420} >)$$

$$B = (28 + 20 < P_{200} > -120 < P_{220} > +27 < P_{400} > +540 < P_{420} > +630 < P_{440} >)$$

$$C = (7 + 10 < P_{200} > -60 < P_{220} > +18 < P_{400} > +270 < P_{420} >)$$

$$D = (< P_{200} > -6 < P_{220} >)$$

$$E = (< P_{200} > +6 < P_{220} >)$$

$$F = (7 + 10 < P_{200} > +18 < P_{400} >)$$

(A2)

The OOP $<P_{200}>$, $<P_{400}>$, $<P_{220}>$, $<P_{420}>$ and $<P_{440}>$ are to be determined by fitting. Introducing the rest of constants:

$$T_i = \frac{2n_g}{n_g + n_i}; \quad T_{ii} = \frac{2n_i}{n_g + n_i}; \quad i=x,z \tag{A3}$$

$$a = \frac{2\alpha_\perp + \alpha_{zz}}{3}; \quad b = \alpha_{zz} - \alpha_\perp \tag{A4}$$

$$m_1 = \frac{2\pi(n_z - n_y)}{\lambda_{scattered}} \quad m_2 = \frac{2\pi(n_z - n_y)}{\lambda_{incident}} \tag{A5}$$

$$R_{iso} = \frac{3b^2}{45a^2 + 4b^2} \tag{A6}$$

Here, n_z and n_y represent the principal refractive indices of the liquid crystal and n_g is the refractive index of the glass plate. $\lambda_{incident}$ and $\lambda_{scattered}$ are the wavelength of the incident and Raman scattered light, respectively. The depolarization ratio, measured in the isotropic phase R_{iso}, provides the relation between a and b which simplifies the Eqs. (A1). The average and the anisotropy of the diagonal Raman tensor are expressed as a and b in Eq. (A4), respectively. In the uniaxial approximation, the relationship $\alpha_\perp = \alpha_{xx}' = \alpha_{yy}'$ is valid. h is the thickness of the liquid crystal cell.

Since the confocal Raman setup requires optical objectives to focus and collect the light in the sample, the experimental data I_{ij}^{exp} must be corrected taking refraction into account before the fitting procedure is performed [33, 57, 58].

$$I_{ij}^{exp}(\omega) = \frac{I_{ij}(\omega)}{n_i(\omega)^2} \tag{A7}$$

Where

$$n_i(\omega) = \frac{n_i n_j}{\sqrt{n_j^2 \cos^2 \omega + n_i^2 \sin^2 \omega}} \text{ for } \{j=z, i=y\} \text{ or } \{i=z, j=y\} \tag{A8}$$

In the particular case $<P_{220}> = <P_{420}> = <P_{440}> = 0$, the expression (A1) is indeed simplified and takes the form of the equations previously presented by Hayashi *et al.* for uniaxial liquid crystals [33].

APPENDIX B: ABOUT THE RAMAN MODELS AND THE OOP

One of the more relevant points to correctly determine the OOP of liquid crystalline systems is directly concerned with the optical anisotropy intrinsic in these materials. Based on the results of Lax and Nelson about the electromagnetic field in anisotropic media [57, 58], Jen *et al.* corrected the intensity Raman response in liquid crystals by refractive indices effects [5]. Here, the optical anisotropy was introduced for the first time in these materials to obtain more precise and reliable OOP. Eq. (A7) expresses the general form the correction factor takes, $(1/n_i^2)$.

In the case of nematics, the correction factor takes this simple form since its mesophase resembles a more liquid-like structure [5, 35]. In contrast, smectics can be better described as liquid-crystalline-like structures and a more adequate correction factor must be taken into account. Hayashi *et al.* [32] introduced the correct factor according to the smectic structure (see Eq. (A8)), widely used in anisotropic crystals [59], and depends on the angular variable ω. The influence of this correction factor in the recent theoretical models proposed by Jones *et al.* and Hayashi *et al.* [35, 29] to obtain the OOP is studied here for the SmA* phase of 9HL. The results are presented in Fig. 16.
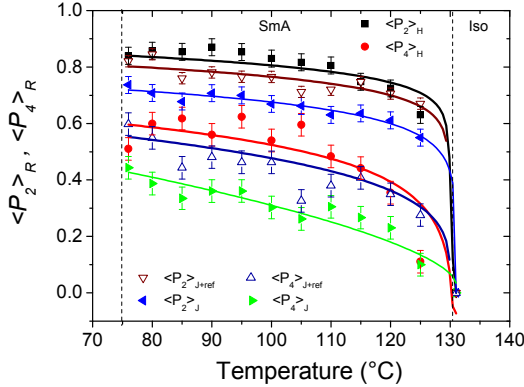

FIG. 16 (Color online) Influence of the optical anisotropic correction factors in the OOP of 9HL. The model proposed by Hayashi *et al.* ($<P_n>_H$) and Jones *et al.* ($<P_n>_{J+ref}$) are in good agreement when the I_{ij}^{exp} is corrected by the same factor, Eq. (A8). On the contrary, if this factor is taken in a simpler form, the $<P_n>_J$ and $<P_n>_{J+ref}$ values differ dramatically.

One can readily see (Fig. 16) the impact of the correction factor (Eq. (A8)) in the OOP after correcting I_{ij}^{exp} in the SmA* phase of 9HL. When Hayashi *et al.* and Jones *et al.* models are corrected by Eq. (A8), the results are quite comparable since de difference in the OOP is about $\Delta<P_n> \approx 0.03$. In this case, both methods yield a value $<P_2> \approx 0.8$ at the SmA*–SmC* phase transition, this is the value reported at the transition of the complete unwounded 9HL in Ref. [28]. Since we are measuring the OOP in a SSFLC configuration, the values reported here correspond to the OOP of the unwounded state of 9HL. On the contrary, assuming a simpler correction factor like the one reported for nematics [5, 35], the experimental results do not reproduce $<P_2> \approx 0.8$ at the transition. In conclusion, the correction factor introduced by Hayashi *et al.* (Eq. (A8)) is required in smectic liquid crystals.

In Fig. 16, one can note a small difference in the values of the OOP $<P_n>_H$ and $<P_n>_{J+ref}$ ($\Delta<P_n> \approx 0.03$) after correcting I_{ij}^{exp} by Eq. (A8). This is not surprising since one can demonstrate that the model introduced by Jones *et al.* corresponds to a particular case of the Hayashi *et al.* model. Here, one can drastically assume that both the birefringence ($\Delta n \approx 0$) and the transmission ($T_i = T_{ii} \approx 1$) coefficients have a negligible contribution to the Raman response. Under these conditions, the system of equations in Hayashi's model can be reduced to the set of equations presented by Jones *et al.*

In Hayashi's model one assumes the principal components of the Raman tensor α_{zz}' and α_{xx}' to be not temperature dependent. Any internal variation with temperature T of the liquid crystal system effecting the Raman signal is taken into account through the variation of the refractive indices $n_z(T)$ and $n_y(T)$ with T (*i.e.* $\Delta n\,(T)$, $T_i\,(T)$, $T_{ii}\,(T)$).

In Jones's model the differential polarizability ratio $r\,(T)$ is defined as $r = \alpha_{xx}'(T)/\alpha_{zz}'(T)$ and is introduced to include any variation with temperature of the Raman signal in the liquid crystal. In a first approximation, the polarizability $\alpha(T)$ can be expressed in terms of the refractive indices of the medium $\alpha(n_z(T), n_y(T))$ [45], so one could assume that the derivative polarizability $\alpha_{ii}'(T)$ follows a similar trend. Hence, the behaviour of the refractive indices with T dictates the magnitude of the correction in the Raman intensity.

The assumption that r is temperature dependent is a quite reasonable choice in Jones's model. Nevertheless one must be aware that this model takes into account variation of $r\,(n_z(T,)\,n_y(T))$ through the approximation of a model for the polarizability [45], while in Hayashi's model these variations comes directly from $n_z(T)$ and $n_y(T)$. Therefore, small differences in the values of the OOP obtained from both models are expected, Fig. 16.

Finally, for a complex structure with positional and orientational order (smectics), the direct inclusion of the variation coming from $n_z(T)$ and $n_y(T)$ in the Hayashi's model gives adequate and precise information to correct the Raman response $I_{ij}\,(\omega)$. While the Jones's model, through the variable r (which indirectly includes the temperature dependence of $n_z(T)$ and $n_y(T)$), gives a quite good approximation to obtain the OOP Fig. 16 [7, 35, 60]. When r is assumed to be constant in the Jones's model, *i.e.* n_z and n_y independent of T, Southern et al. showed that for a nematic the values of $<P_4>$ were anomalously low [60]. This confirms the importance and necessity to include the correct temperature dependent parameters in the theoretical model in order to determine the OOP of a liquid crystal correctly.

APPENDIX C: REFRACTIVE INDICES

An important part of the present Raman study (A1) is to know a priori the principal refractive indices of a particular mesophase. We determined these indices experimentally in the SmA* and SmC* phases using the scanning conoscopy method proposed by Bitri *et al.* [61]. In general words, the optical retardation δ_k is measured as a function of the scanning angle σ. Typical interference profiles obtained by this method as well as their fitted curves are presented in Figure 17:
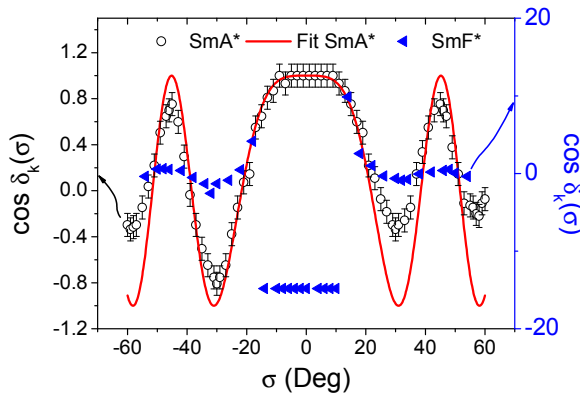

FIG. 17 (Color online) Scanning conoscopy profiles of 9HL. The experimental retardation is shown as a) open dots in the SmA* phase and b) blue triangles in the SmF* phase. The solid red line represents

the best fit to the experimental points in the SmA* phase. A homeotropically aligned 20 μm cell was used in these experiments.

In the homeotropic cell, both the SmA* and helical SmC* phases looked optically uniaxial and exhibited rather similar scanning profiles. As a rule, the profiles measured in an optically uniaxial phase must have a maximum equal to 1 around $\sigma = 0$, *i.e.* zero retardance for normally incident light. In contrast, it can happen that an anisotropic local structure around the layer normal, due to the rotation of the local biaxial structure, appears. This induce a rotation of the light polarization and yields a maximum around $\sigma = 0$ different from 1, as pointed out by Bitri *et al.* [61]. The refractive indices obtained using this method are presented in Fig. 18.
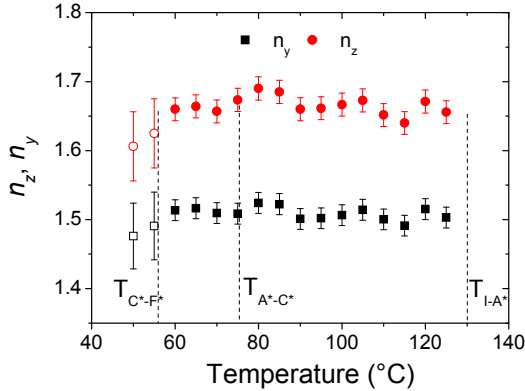

FIG. 18 (Color online) Principal refractive indices of 9HL obtained using scanning conoscopy. The experimental data shown in the SmF* phase represent only the apparent values of the refractive indices calculated in the uniaxial approximation.

APPENDIX D: SMECTIC PHASES OF 9HL RECONSIDERED

The first calorimetric (DSC) measurements carried out on 9HL showed that this material exhibits only the SmA* and SmC* phases. These and other experiments showed that the SmA*–SmC* transition must be second order. The phase sequence in 9HL was reported to be: Iso–130 °C–SmA*–75 °C–SmC*–40°C–Crystalline [12, 18, 27, 28]. Here, we present the experimental proof of the existence of another intermediate smectic phase in this material.

The scattering diffraction pattern shown in Fig. 19 was measured at a temperature of 45 °C and is substantially different from those observed in Fig. 8. In both figures (Fig. 19 and Fig. 8) one clearly observes the usual broad peak around $q_y \approx 1.5$ Å^{-1}, which is commonly found in nematic and smectics liquid crystals in the q_y direction. One notes that the signal around $q_z \approx 1.5$ Å^{-1} is obviously several times smaller than the signal integrated along q_y, therefore a secondary weak reflection is easier to observe around this q_z.
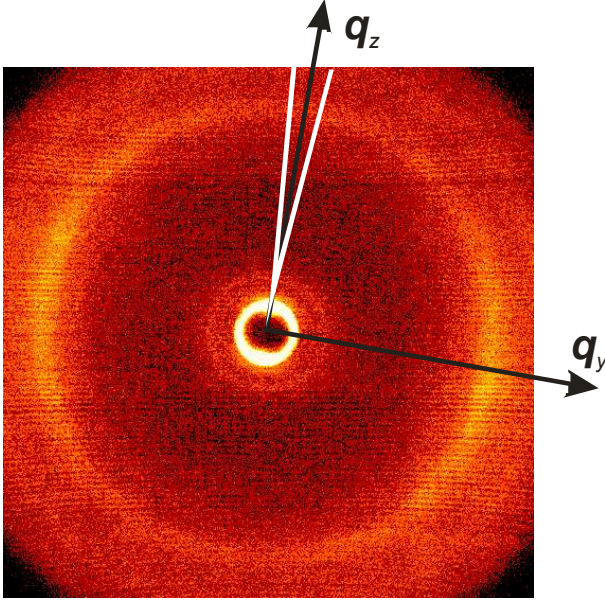
FIG. 19 (Color online) Scattering profile observed in the SmF* phase of 9HL. Note the secondary outer ring in the WAXS signal as well as the sharpness of the diffuse ring. This picture is distinctly different from those observed in the SmA* and SmC* phases (see Fig. 8). $I(q_z)$ is obtained integrating along the q_z axis inside the region limited by the white triangle.

The integrated $I(q_z)$ scattered x-ray signal along the layer normal **k** is rather similar in the SmA* and SmC* phases as shown in Fig. 20. In contrast, at temperatures below $T = 56$ °C the peak at $q_z \approx 1.5$ Å^{-1} becomes sharper and a secondary peak appears at $q_z \approx 1.7$ Å^{-1}. The sharpness of this peak is as a signature of the SmF* phase attributed to the packing of the molecules inside the layers [62-64].
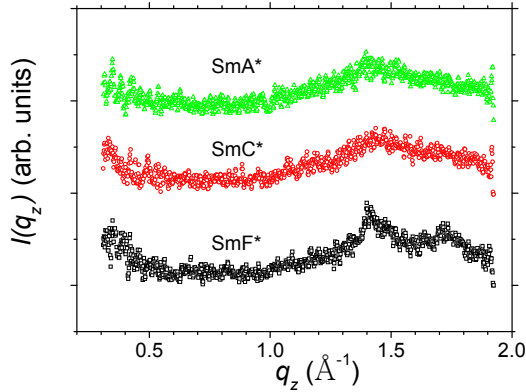

FIG. 20 (Color online) Scattering profiles along **q**$_z$ in the SmA*, SmC* and SmF* phases, respectively. Note the appearance of a secondary peak in the SmF* phase around $q_z = 1.7$ Å^{-1}.

A phase transition from the SmC* phase to a more ordered phase is also indicated by the temperature variation of the rotational viscosity γ. Polarization reversal measurements can also be used to determine γ in the whole interval from the SmA* to the crystalline phase. The details of that method are described in detail in ref. [65, 66]. Applying an electrical field of 35 V/µm across the cell of 1.6 µm and a triangular wave with the frequency of 20 Hz we have determined the temperature variation of γ, shown in Fig. 21:
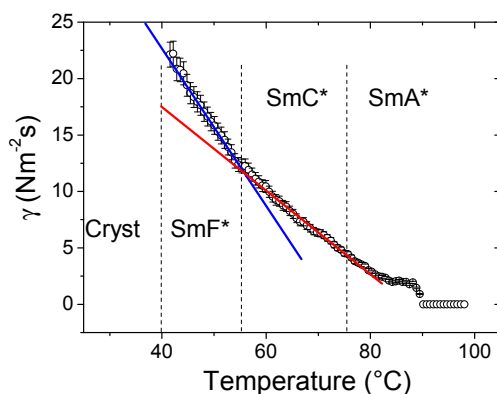
FIG. 21 (Color online) Rotational viscosity of 9HL determined from polarization reversal current measurements.

The phase transition from the SmC* into a more ordered phase is usually accompanied by an abrupt increase in the rotational viscosity [67]. At first sight, the curve presented in Fig. 21 seems to be continuous across the smectic phases. However, a small discontinuity at the SmC*–SmF* phase transition is visible. Instead of an abrupt change of γ at the transition, one observes a discontinuity in the slope of the SmC*–SmF* transition.

At 56 °C, the scanning conoscopy experiments also indicate that there is a transition from the optically uniaxial helical SmC* into a phase with a local biaxial structure, as shown in Fig. 17. This information together with the evidence presented in the x-ray analysis, leads us to conclude that the intermediate phase between the SmC* and the crystalline phase might be the SmF*, and that the SmC*–SmF* transition is possibly second order since the change in viscosity is continuous and rather small. The revised phase sequence of 9HL is then: Iso–130 °C–SmA*–75 °C–SmC*–56 °C–SmF*–40°C–Crystal.

REFERENCES

[1] P.G. de Gennes and J. Prost, *The Physics of Liquid Crystals* (2nd ed. Clarendon Press, Oxford, 1993)
[2] C. Zannoni, in *The molecular physics of liquid crystals*, (G. R. Luckhurst and G. W. Gray (Eds). Academic Press, London 1979)
[3] A. J. Leadbetter and E. K. Norris, Mol. Phys., **38**, 669 (1979)
[4] P. Davidson, D. Petermann, and A. M. Levelut, J. Phys. II, **5**, 113 (1995)
[5] S. Jen, N. A. Clark and P. S. Pershan, J. Chem. Phys., **66**, 4635 (1977)
[6] S. D. Durbin and Y. R. Shen, Phys. Rev. A, **30**, 1419 (1984)
[7] A. Sanchez-Castillo, M. A. Osipov and F. Giesselmann, Phys. Rev. E, **81**, 021707 (2010)
[8] G. R. Luckhurst and R. N. Yeates, J. Chem. Soc. Faraday Trans. II, **72,** 996 (1976)
[9] C. Zannoni, *Polarized Spectroscopy of Ordered Systems*, (Kluwer Academic Publishers, 1988)
[10] A. de Vries, Mol. Cryst. Liq. Cryst., **41**, 27 (1977)
[11] M. Krueger and F. Giesselmann, Phys. Rev. E, **71**, 041704 (2005)
[12] S. Bezner, M. Krueger, V. Hamplová, M. Glogarová, and F. Giesselmann, Phys. Rev. E, **126**, 054902 (2007)
[13] A. de Vries, A. Ekachai and N. Spielberg, Mol. Cryst. Liq. Cryst., **49**, 143 (1979)
[14] J. P. F. Lagerwall and F. Giesselmann, Chem. Phys. Chem., **7**, 20 (2006)
[15] A. de Vries, J. Chem. Phys., **71**, 25 (1979)

[16] A. de Vries, Mol. Cryst. Liq. Cryst., **49**, 179 (1979)

[17] S. T. Lagerwall, P. Rudquist and F. Giesselmann, Mol. Cryst. Liq. Cryst., **510**, 148 (2009)

[18] F. Giesselman, P. Zugenmaier, I. Dierking, S. T. Lagerwall, B. Stebler, M. Káspar, V. Hamplová and M. Glogarová, Phys. Rev. E, **60**, 598 (1999)

[19] Y. P. Panarin, V. Panov, O. E. Kalinovskaya and J. K. Vij, J. Mater. Chem., **9**, 2967 (1999)

[20] J. Naciri, J. Ruth, G. Crawford, R. Shashidhar and B. R. Ratna, Chem. Mater., **7**, 1397 (1995)

[21] U. Manna, J. K. Song, Y. P. Panarin, A. Fukuda and J. K. Vij, Phys. Rev. E, **77**, 041707 (2008)

[22] N. Hayashi, T. Kato, A. Fukuda, J. K. Vij, Y. P. Panarin, J. Naciri, R. Shashidhar, S. Kawada and S. Kondoh, Phys. Rev. E, **71**, 041705 (2005)

[23] N. Hayashi, A. Kocot, M. J. Linehan, A. Fukuda, J. K. Vij, G. Heppke, J. Naciri, S. Kawada and S. Kondoh, Phys. Rev. E, **74**, 051706 (2006)

[24] J. P. F. Lagerwall, F. Giesselmann and M. D. Radcliffe, Phys. Rev. E, **66**, 031703 (2002)

[25] N. Kasai and M. Kakudo, *X-Ray Diffraction by Macromolecules* (Springer, 2005)

[26] M. A. Linne, *Spectroscopic Measurement*, (Academic Press, 2002)

[27] M. Káspar, V. Hamplová, S. A. Pakhomov, A. M. Bubnov, F. Guittard, H. Sverenyak, I. Stibor, P. Vanek and M. Glogarová, Liq. Cryst., **24**, 599 (1999)

[28] A. Marchetti, V. Domenici, V. Novotna, M. Lelli, M. Cifelli, A. Lesage and C. A. Veranici, Chem. Phys. Chem, **11**, 1641 (2010)

[29] H. Yoon, D. M. Kooijman, K. Ayub, R. P. Lemieux and S. Kumar, Phys. Rev. Lett., **106**, 087801 (2011)

[30] H. S. Chang, S. Jaradat, H. F. Gleeson, I. Dierking and M. A. Osipov, Phys. Rev. E, **79**, 061706 (2009)

[31] J. C. Roberts, N. Kapernaum, Q. Song, D. Nonnenmacher, K. Ayub, F. Giesselmann, R. P. Lemieux, J. Am. Chem. Soc., **132**, 364 (2010)

[32] N. Hayashi and T. Kato, Phys. Rev. E, **63**, 021706 (2001)

[33] N. Hayashi, T. Kato, T. Aoki, T. Ando, A. Fukuda and S. S Seomun, Phys. Rev. E, **65**, 041714 (2002)

[34] N. Hayashi, T. Kato, T. Ando, A. Fukuda, S. Kawada and S. Kondoh, Phys. Rev. E, **68**, 011702 (2003)

[35] W. J. Jones, D. K. Thomas, D. W. Thomas and G. Williams, J. Mol. Struct., **708**, 145 (2004)

[36] V. Gurp, Colloid. Polym. Sci., **273**, 607 (1995)

[37] C. D. Southern, P. D. Brimicombe, S. D. Siemianowski, S. Jaradat, N. Roberts, V. Görtz, J. W. Goodby and H. F. Gleeson, Eur. Phys. Lett., **82**, 56001 (2008)

[38] P. Oswald, *Smectic and Columnar Liquid Crystals - Concepts and Physical Properties Illustrated By Experiments*, (Taylor and Francis Group, 2006)

[39] N. Kapernaum and F. Giesselmann, Phys. Rev. E, **78**, 062701 (2008)

[40] M. J. Frisch, *et al., Gaussian 98 (Gaussian, Inc., Pittsburgh, PA)*, (1998).

[41] A.D. Becke, J.Chem.Phys. **98**, 5648 (1993)

[42] A. P. Scott and L. Radom, J. Phys. Chem., **100**, 16502 (1996)

[43] D. Krüerke, Dissertation, (1999); M. Kawaida, T. Yamaguchi and T. Akahane, Jap. J. Appl. Phys., **28**, L1602 (1989)

[44] A. Kumar, A. Phys. Pol. A, **112**, 1213 (2007)

[45] B. J. Zywucki and W. Kuczynsky, IEEE J. Trans. Dielec. Elec. Insul., **8**, 512 (2001)

[46] W. M. Kaganer, B. I. Ostrovskii and W. H. Jeu, Phys. Rev. A, **44**, 8158 (1991)

[47] A. Primak, M. Fisch and S. Kumar, Phys. Rev. E, **66**, 051707 (2002)

[48] W. Maier and A. Saupe , Z. Naturforsch., **15a**, 287 (1960)

[49] S. Y. Yakovenko, A. A. Minko and J. Pelzl, Ferroelec., **245**, 17, (2000)

[50] M. Constant and D. Decoster, J. Chem. Phys., **76**, 1708 (1982)

[51] N. Bielejewska, E. Chrzzumnicka, E. Mykowska, R. Przybylski, M. Szybowicz, K. Wladysiak and D. Bauman, A. Phys. Pol. A, **110**, 777 (2006)

[52] C. P. Lafrance, A. Nabet, R. E. Prud'homme and Michel Pézolet, Can. J. Chem., **73**, 1497 (1995)

[53] S. E. Yakovenko, Spektroskopii, **47**, 779 (1987)

[54] E. M. Averyanov and M.A.Osipov, Sov. Phys. Usp., **33**, 365 (1990**)**

[55] S. E. Yakovenko, V. I. Naumenko, A. A. Min´ko and N. M. Ksenofontova, Spektroskopii, **37**, 301 (1982)

[56] I. I. Penchev and I. N. Dozov, Mol. Cryst. Liq. Cryst., **73**, 267 (1981)

[57] M. Lax and D.F. Nelson, Phys. Rev. B, **4**, 3694 (1971)

[58] M. Lax and D.F. Nelson, J. Opt. Soc. Am., **65**, 668 (1975)

[59] A. Yariv, P. Yeh, *Optical Waves in Crystals*, (John Wiley and Sons, Inc. Publications, 2003)

[60] C. D. Southern and H.F. Gleeson, Eur. Phys. J. E, **24**, 119 (2007)

[61] N. Bitri, A. Gharbi and J. P. Marcerou, Phys. B, **403**, 3921 (2008)

[62] J. J. Benattar, F. Moussa and M. Lambert, J. Phys., **41**, 1371 (1980)

[63] J. J. Benattar, J. Doucet, M. Lambert and A. M. Levelut, Phys. Rev. A, **20**, 2505 (1979)

[64] A. J. Leadbetter, J. P. Gaughan, B. Kelly, G. W. Gray and J. Goodby, J. Phys., **40**, C3-178 (1979)

[65] S. Kimura, S. Nishiyama, Y. Ouchi, H. Takezoe and A. Fukuda, Jap. J. Appl. Phys., **26**, L255 (1987)

[66] I. Dierking, F. Giesselmann, P. Zugenmaier, G. Pelzl, and P. Schiller, Cryst. Res. Tech., **27**, 727 (1992)

[67] I. Dierking, F. Giesselmann, J. Kußerow and P. Zugenmaier, Liq. Cryst., **17**, 243 (1994)